Preprint Title	Microbubbles Decorated with Dendronized Magnetic Nanoparticles for Biomedical Imaging. Effective Stabilization via Fluorous Interactions
Authors	Da Shi, Justine Wallyn, Dinh-Vu Nguyen, Francis Perton, Delphine Felder-Flesch, Sylvie Bégin-Colin, Mounir Maaloum and Marie Pierre Krafft
Article Type	Full Research Paper
Supporting Information File 1	Supporting_Shi. BJNano.29.06.19.docx; 137.0 KB
ORCID® iDs	Marie Pierre Krafft - https://orcid.org/0000-0002-3379-2783

Microbubbles Decorated with Dendronized Magnetic Nanoparticles for Biomedical Imaging. Effective Stabilization via Fluorous Interactions

Da Shi[1], Justine Wallyn[1], Dinh-Vu Nguyen[2], Francis Perton[2], Delphine Felder-Flesch[2], Sylvie Bégin-Colin[2], Mounir Maaloum[1], Marie Pierre Krafft[1*]

[1]Institut Charles Sadron (CNRS), University of Strasbourg, 23 rue du Loess. 67034 Strasbourg (France)

[2]Institut de Physique et de Chimie des Matériaux de Strasbourg (IPCMS), University of Strasbourg, 23 rue du Loess. 67034 Strasbourg (France)

*Corresponding author:
Dr. Marie Pierre Krafft
krafft@unistra.fr

Abstract

Dendrons fitted with three oligoethylene glycol (OEG) chains, one of which carrying a fluorinated or hydrogenated end group, and bearing a bisphosphonate polar head ($C_nX_{2n+1}OEG_8Den$, X = F or H; n = 2 or 4) were synthesized and grafted on the surface of iron oxide nanoparticles (IONPs) for microbubble-mediated imaging and therapeutic purposes. The size and stability of the dendronized IONPs ($IONP@C_nX_{2n+1}OEG_8Den$) in aqueous dispersions were monitored by dynamic light scattering. Investigation of the spontaneous adsorption of $IONP@C_nX_{2n+1}OEG_8Den$ at the interface between air - or air saturated with perfluorohexane - and an aqueous phase establishes that exposure to the fluorocarbon gas markedly increases the rate of adsorption of the dendronized IONPs to the gas/water interface and decreases the equilibrium interfacial tension. This suggests that fluorous interactions are at play between the supernatant fluorocarbon gas and the fluorinated end groups of the dendrons. Furthermore, small, stable perfluorohexane-stabilized microbubbles (MBs) with a dipalmitoylphosphatidylcholine (DPPC) shell that incorporates $IONP@C_nX_{2n+1}OEG_8Den$ (DPPC/Fe molar ratio 28:1) were prepared and characterized using both optical microscopy and an acoustical method of size determination. The dendrons fitted with fluorinated end groups lead to smaller and more stable MBs than those fitted with hydrogenated groups. The most effective result is already obtained with C_2F_5, for which MBs, ~1.0 μm in radius, reach a half-life of ~6.0 h. An atomic force microscopy investigation of spin-coated mixed films of $DPPC/IONP@C_2X_5OEG_8Den$ combinations (molar ratio 28:1) shows that the IONPs grafted with the fluorinated dendrons are located within the phospholipid film, while those grafted with the hydrocarbon dendrons are completely absent from the phospholipid film.

Keywords: fluorinated dendron; fluorocarbon; iron oxide nanoparticle; magnetic nanoparticle; microbubble; diagnostic imaging.

Introduction

Microbubbles (MBs), that is, micron-size gas particles dispersed in an aqueous medium, are clinically used as contrast agents for ultrasound imaging, including molecular imaging, and actively investigated for surgical ablation, targeted drug and gene delivery [1]. They are also being examined for use, in conjunction with focused ultrasound, and under magnetic resonance imaging guidance, for achieving blood/brain and blood/tumor barrier crossing of drugs [2]. Medical MBs have a shell consisting of surfactants, phospholipids, or polymers, and are most generally stabilized by a fluorocarbon gas [3] that acts as an osmotic agent [4, 5] and as a co-surfactant to phospholipids [6] and block co-polymers [7].

Nanoparticles can be attached to the bubble shells to extend their diagnostic and therapeutic potential by combining multimodal imaging, drug or gene delivery, and/or enhancement and control of the acoustic signal for energy deposition, as for sonothrombolysis or ablation surgery. MBs incorporating iron oxide nanoparticles (IONPs) are sought after as dual contrast agents for ultrasound and magnetic resonance imaging [8] and drug delivery [9]. The shells of the presently available MBs incorporating IONPs are often made of polymers. For example, ultra-small superparamagnetic iron oxide nanoparticles were embedded in the wall of poly(butyl cyanoacrylate)-based MBs allowing the monitoring of blood-brain barrier penetration [10]. Soft-shell colloids called lipospheres have also been reported for enhanced gene and drug delivery [9, 11, 12]. These lipospheres consist of gas-filled spheres coated by a film of soybean oil that encloses the cargo of nanoparticles and is itself contained within a film of phospholipids [11]. Both polymer-shelled MBs and lipospheres have some advantages and some limitations [13]. In both cases, the shells can be custom-made to enhance stability, circulation duration, drug loading capacity and release rate, targeting to and fusion with cell membranes [11]. Both types of constructs are generally more stable, but less echogenic than ‘‘true’’ gas microbubbles, due to the dampening effect of the polymer shell or oil contained in the phospholipid coating [11, 13]. One important difficulty encountered in the preparation of such magnetic MBs is that IONPs rapidly aggregate in aqueous media [13]. Commercially available 50 nm magnetic IONPs coated with phospholipids allowed preparation of MBs that enabled transfection of neuroblastoma cells with a generic fluorescent small interfering RNA under magnetic and ultrasound fields [14].

In the present work, we have incorporated IONPs coated by dendritic phosphonates bearing oligoethylene glycol (OEG) chains in the phospholipid shell of the MBs. Dendritic phosphonates are effective anchoring agents due to the covalent PO-metal bonds that stabilize aqueous dispersions of IONPs [15, 16]. Such dendronized IONPs have been investigated for hyperthermia and MRI owing to their increased stability in aqueous media and biocompatibility [16, 17]. An even stronger anchoring agent consisting of a dendron structure bearing a bisphosphonate polar head provided increased colloidal stability in physiological media [18]. To our knowledge, the implementation of dendronized IONPs in phospholipid-shelled MBs has never been reported.

We report here the preparation of perfluorohexane (*F*-hexane)-stabilized MBs with a shell of dipalmitoylphosphatidylcholine (DPPC) that incorporates IONPs grafted with OEG bisphosphonate-headed dendrons. Four dendrons were synthesized and investigated that feature two phosphonic acids and three OEG chains, including a longer one in the para position. The latter was fitted with a fluorinated (C_2F_5 or C_4F_9) or a hydrogenated (C_2H_5 or C_4H_9) end group ($C_nX_{2n+1}OEG_8Den$, X = F and H; $n = 2$ and 4, Scheme 1). First, we present the synthesis and characterization of IONPs grafted with the selected dendrons (IONP@$C_nX_{2n+1}OEG_8Den$). Second, we report the

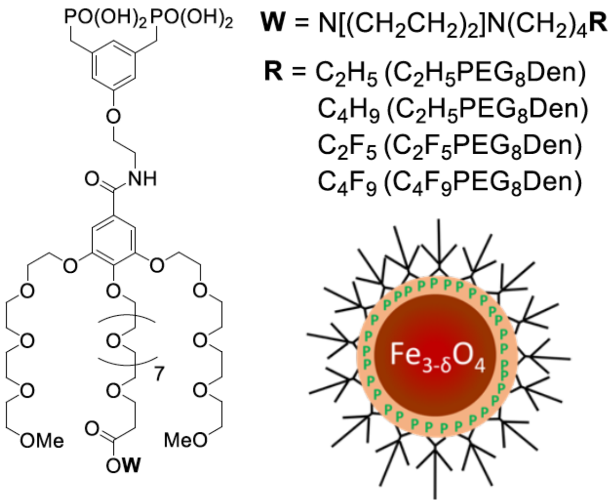

Scheme 1: a) Molecular structure of the dendrons investigated (C_nX_{2n+1}OEG$_8$Den, X = F or H; n = 2 and 4); b) Schematic representation of a dendronized IONP showing the anchoring of the bisphosphonate function on the iron oxide.

adsorption kinetics of IONP@C_nX_{2n+1}OEG$_8$Den at the interface between air, or *F*-hexane-saturated air, and water. In a third section, we discuss the size and stability characteristics of *F*-hexane-stabilized MBs shelled with DPPC and incorporating IONP@C_nX_{2n+1}OEG$_8$Den. A fourth section reports an atomic force microscopy (AFM) study that demonstrates that the location of the dendronized nanoparticles in the phospholipid film strongly depends on the nature of the terminal group.

Results and Discussion

Synthesis and grafting of dendrons on iron oxide nanoparticles

The OEG dendrons were synthesized as described in the *Experimental Part*. Briefly, the piperazine scaffold was selected as an appropriate template to introduce the perfluoroalkylated or alkylated chain on a generation 1 bisphosphonic dendron bearing three OEG chains [19]. In order to facilitate the insertion and increase the visibility of the perfluoroalkylated (or alkylated) end group into the microbubble wall, the central OEG chain carrying the piperazine moiety has been lengthened (Scheme

1a). A multistep chemical sequence allowed production of bisphosphonate dendrons in reasonable yield (55 to 80%). IONPs (mean diam. 9.0 ± 0.9 nm) were synthesized by thermal decomposition of iron (II) stearate in the presence of oleic acid in dioctylether, which allows enhanced control of the size, morphology, and composition of the IONPs [20]. The four dendrons were grafted on the magnetic IONPs by direct exchange of the ligand (oleic acid) according to [21]. The excess dendron was removed by ultrafiltration. The grafting of the dendrons on the IONPs was assessed by infrared spectroscopy (IR), which showed significant reduction of oleic acid alkyl bands (2926-2850 cm^{-1}) and appearance of OEG signal (1096 cm^{-1}) (*Supporting Information* Fig. S1). The grafting of the dendrons on the IONPs was also confirmed by dynamic light scattering (DLS, Fig. 1). The hydrodynamic mean diameter of IONP@$C_2X_5OEG_8$Den (X = F or H) was ~37 nm, which is a significant increase as compared to the mean diameter of oleic acid-covered IONPs (~10 nm, Fig. S2), and was ascribed to the corona formed by the OEG chains. The mean diameters of IONP@$C_4X_9OEG_8$Den were larger, ~95 nm and ~200 nm respectively, revealing that aggregation occurs in aqueous media due to the hydrophobicity of the end group.

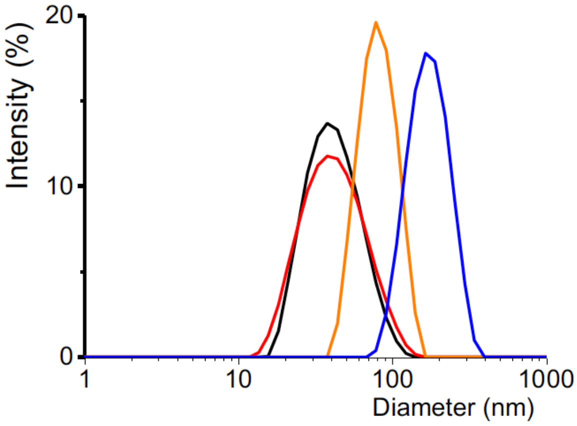

Figure 1. Hydrodynamic diameter distributions of IONPs grafted with dendrons: $C_2H_5OEG_8$Den (38 ± 1 nm, black), $C_2F_5OEG_8$Den (37 ± 1 nm, red), $C_4H_9OEG_8$Den (95 ± 12 nm, orange), $C_4F_9OEG_8$Den (197 ± 15 nm, blue) in aqueous dispersions (Fe conc. 0.05 mg mL^{-1}).

This did fortunately not preclude performing the adsorption kinetics studies. Altogether, the OEG chains through the dendritic structure were found to confer excellent dispersibility and stability to the IONPs [21].

Adsorption kinetics of dendronized nanoparticles at the gas/liquid interface

The adsorption of the dendronized IONPs at the air/water and *F*-hexane-saturated air/water interfaces was first investigated using bubble profile analysis tensiometry. As described in our earlier reports [22], we first confirmed that *F*-hexane taken alone, when it is introduced in the gaseous phase of the tensiometer bubble, adsorbs rapidly to the interface, as indicated by an instant reduction of σ by ~4 mN m^{-1} (from 72 to 68 ± 0.5 mN m^{-1}, Fig. S3). The concentrations of Fe in the IONP dispersions were varied from 10^{-4} to 10^{-1} mol L^{-1}. The variations of the interfacial tension σ over time are collected in Figure 2 and Table I.

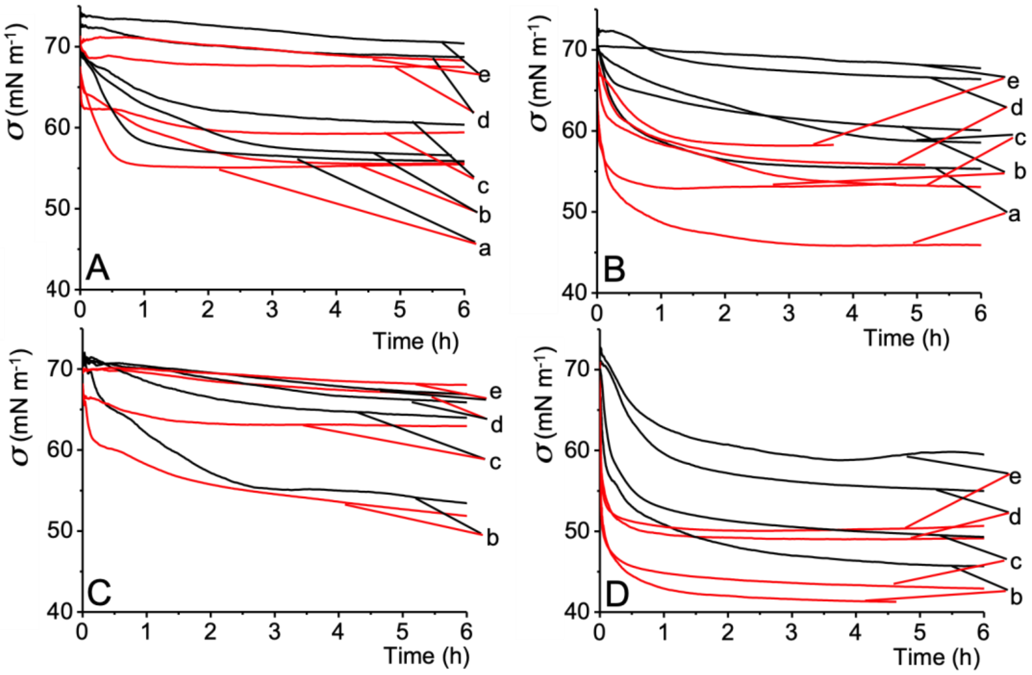

Figure 2. Adsorption kinetics at 25°C of IONPs grafted with various dendrons: A) $C_2H_5OEG_8Den$, B) $C_2F_5OEG_8Den$, C) $C_4H_9OEG_8Den$ and D) $C_4F_9OEG_8Den$, at various Fe concentrations: a) 0.1; b) 0.05; c) 10^{-2}; d) 10^{-3} and e) 10^{-4} mg mL^{-1}. The dendronized IONPs were exposed to air (black) or to *F*-hexane-saturated air (red).

The results show that, not surprisingly, σ decreases with Fe concentration in all cases. The lowest σ values are obtained for the IONPs grafted with the fluorinated dendrons, reflecting their higher hydrophobicity. We also observe that exposure to *F*-hexane has two important consequences on the adsorption of dendronized IONPs. First, the adsorption process is accelerated, and second, the equilibrium interfacial tensions are significantly lowered. We have reported similar effects of the fluorocarbon gas on the adsorption of a range of molecules, including phospholipids [23], polymers [7], proteins [24], biomarkers [25], and of CeO_2 nanoparticles [26]. But the most important finding here is that the fluorocarbon gas affects the adsorption of IONPs differently, depending on whether the dendron carries a fluorinated end group or not. The interfacial tensions at equilibrium σ_{eq} of the dendronized IONP dispersions and characteristic times of adsorption τ of the latter for various Fe concentrations are collected in Table 1. The τ values were determined by fitting the adsorption profiles (Fig. 2) to an exponential decay function. The variations of σ_{eq} versus Fe concentration are plotted in Fig. 3a. The differences, $\Delta\sigma_{eq}$, between σ_{eq} for dendronized IONPs exposed to air and exposed to *F*-hexane-saturated air, are also plotted as a function of Fe concentration (Fig. 3b). $\Delta\sigma_{eq}$ are larger for the fluorinated

Table 1. Characteristic time of adsorption τ (h) and interfacial tension at equilibrium σ_{eq} (mN m^{-1}) of IONPs grafted with hydrogenated or fluorinated dendrons.

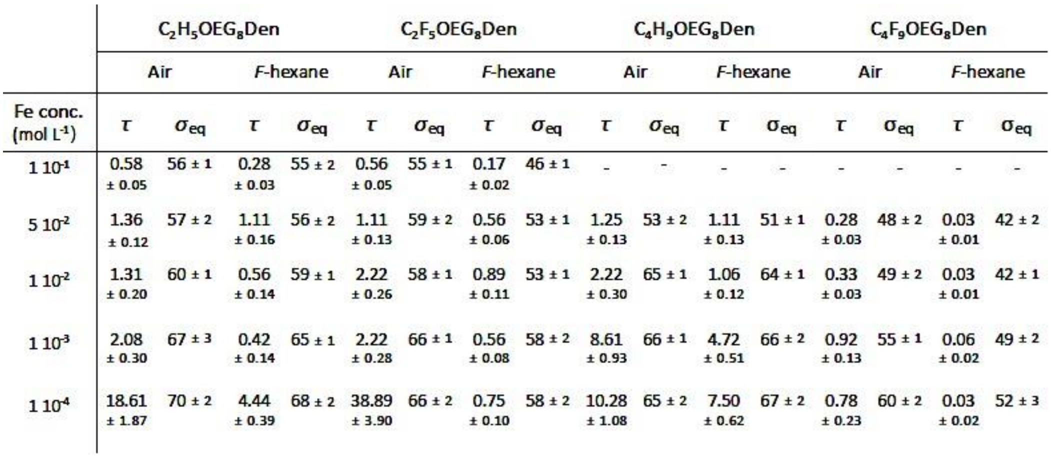

	$C_2H_5OEG_8Den$				$C_2F_5OEG_8Den$				$C_4H_9OEG_8Den$				$C_4F_9OEG_8Den$			
	Air		*F*-hexane		Air		*F*-hexane		Air		*F*-hexane		Air		*F*-hexane	
Fe conc. (mol L^{-1})	τ	σ_{eq}	τ	σ_{eq}	τ	σ_{eq}	τ	σ_{eq}	τ	σ_{eq}	τ	σ_{eq}	τ	σ_{eq}	τ	σ_{eq}
1 10^{-1}	0.58 ± 0.05	56 ± 1	0.28 ± 0.03	55 ± 2	0.56 ± 0.05	55 ± 1	0.17 ± 0.02	46 ± 1	-	-	-	-	-	-	-	-
5 10^{-2}	1.36 ± 0.12	57 ± 2	1.11 ± 0.16	56 ± 2	1.11 ± 0.13	59 ± 2	0.56 ± 0.06	53 ± 1	1.25 ± 0.13	53 ± 2	1.11 ± 0.13	51 ± 1	0.28 ± 0.03	48 ± 2	0.03 ± 0.01	42 ± 2
1 10^{-2}	1.31 ± 0.20	60 ± 1	0.56 ± 0.14	59 ± 1	2.22 ± 0.26	58 ± 1	0.89 ± 0.11	53 ± 1	2.22 ± 0.30	65 ± 1	1.06 ± 0.12	64 ± 1	0.33 ± 0.03	49 ± 2	0.03 ± 0.01	42 ± 1
1 10^{-3}	2.08 ± 0.30	67 ± 3	0.42 ± 0.14	65 ± 1	2.22 ± 0.28	66 ± 1	0.56 ± 0.08	58 ± 2	8.61 ± 0.93	66 ± 1	4.72 ± 0.51	66 ± 2	0.92 ± 0.13	55 ± 1	0.06 ± 0.02	49 ± 2
1 10^{-4}	18.61 ± 1.87	70 ± 2	4.44 ± 0.39	68 ± 2	38.89 ± 3.90	66 ± 2	0.75 ± 0.10	58 ± 2	10.28 ± 1.08	65 ± 2	7.50 ± 0.62	67 ± 2	0.78 ± 0.23	60 ± 2	0.03 ± 0.02	52 ± 3

dendrons than for their hydrogenated analogs (7.0 ± 1.3 vs. 1.1 ± 1.0 mN m^{-1}). This means that, in the presence of the fluorocarbon gas, the surface excess of fluorinated dendrons is higher than for the hydrogenated analogs, or that the fluorinated dendrons form a more densely organized film at the interface. In either way, these results strongly suggest the existence of fluorous interactions between the end group of the dendrons and the supernatant fluorocarbon gas, which facilitate the adsorption of the IONPs at the interface. Although mutual interactions between fluorinated chains are notoriously weak, effective attractive interactions can operate in water and organic solvents. Illustrations of enactment of such interactions comprise partition and segregation of *F*-alkyl chains, on which "fluorous" technologies are based that are used in many synthesis and separation processes [27]. All published cases of such interactions are, however, restricted to liquid/liquid and solid/liquid interfaces [28]. By contrast, the potential of fluorocarbon gases to develop attractive fluorous interactions at the gas/water interface has only be recently demonstrated [25].

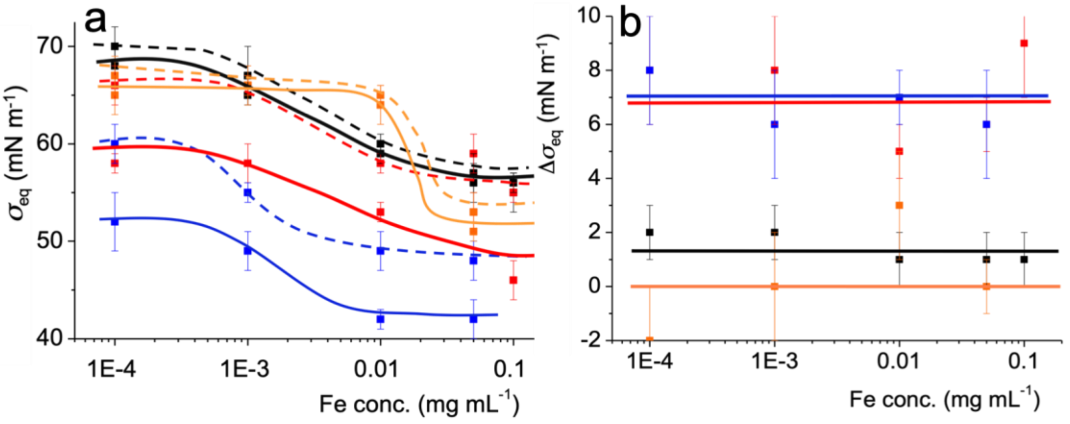

Figure 3. a) Variation of interfacial tension at equilibrium σ_{eq} (25°C) as a function of Fe concentration in dispersions of IONPs grafted with dendrons ($C_2H_5OEG_8Den$: black; $C_2F_5OEG_8Den$: red; $C_4H_9OEG_8Den$: orange and $C_4F_9OEG_8Den$: blue) at the air (dashed) and *F*-hexane-saturated air (solid line)/aqueous phase interface. b) Variation of the difference of σ_{eq} $\Delta\sigma_{eq}$ measured under air and under *F*-hexane-saturated air versus Fe concentration for various IONPs (same color codes).

The $1/\tau$ values increase with Fe concentration (Fig. 4a), except for $C_4F_9OEG_8Den$ in which case adsorption is only slightly increased (under air) or remained constant (under *F*-hexane). In all cases, the adsorption of the IONPs is accelerated by exposure to the *F*-hexane gas. The magnitude of this effect depends on the degree of fluoration of the dendron. The differences $\Delta 1/\tau$ of $1/\tau$ values measured under air or under *F*-hexane exposure are collected for each dendronized IONP in Fig. 4b. The largest $\Delta 1/\tau$ values are obtained for the dendron fitted with the C_4F_9 end group, which indicates that the strength of the interactions between *F*-hexane and the terminal group increases with the number of fluorinated carbons of the latter.

Preparation and characterization of microbubbles incorporating dendronized iron oxide nanoparticles

The size and stability characteristics of *F*-hexane-stabilized microbubbles prepared with DPPC and dendronized IONPs were investigated by optical microscopy and ultrasound wave attenuation analysis. MBs stabilized by a shell of DPPC only were

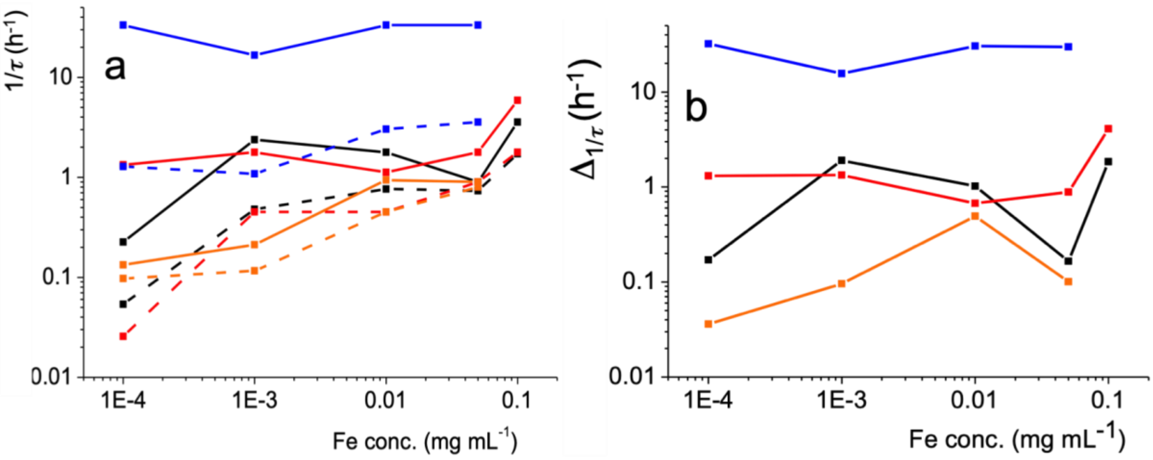

Figure 4. a) Variation of the inverse of the characteristic time of adsorption $1/\tau$ of IONPs grafted with dendrons ($C_2H_5OEG_8Den$: black; $C_2F_5OEG_8Den$: red; $C_4H_9OEG_8Den$: orange; $C_4F_9OEG_8Den$: blue) at the air (dashed) and *F*-hexane-saturated air (solid line)/aqueous phase interface. b) Variation of the differences $\Delta 1/\tau$ of $1/\tau$ values measured under air and *F*-hexane-saturated air as a function of Fe concentration (same color codes).

investigated for comparison. Our acoustic device measures the variation of the attenuation coefficient of an ultrasound wave as a function of its frequency at the initial measuring time in the measuring cell (Experimental Section). The change of the radius distributions over time is calculated from the attenuation curves. The bubble fraction is plotted against time, allowing determination of the half-life of the bubbles [25]. The size and stability characteristics of the MBs incorporating the dendronized IONPs in their DPPC shell are provided in Table 2 and Figure 5. The addition of dendronized IONPs led to a significant change in MB mean size and size distribution for all the dendronized IONPs investigated, confirming their presence in the MB shell. A mean radius as small as 1.0 ± 0.2 µm was obtained with the fluorinated dendrons $C_2F_5OEG_8Den$ and $C_4F_9OEG_8Den$, comparable to that measured for a non-dendronized DPPC shell. By comparison, use of hydrogenated dendrons led to an increase in MB mean radius. The stability of the MBs prepared with the fluorinated IONPs was also significantly higher than for those prepared with non-fluorinated NPs, and, at least for $C_2F_5OEG_8Den$ comparable to that of DPPC (6.1 ± 0.9 h vs. 6.8 ± 0.5, respectively; Table 2, Fig. 6). These differences in behavior obtained whether the dendron has a fluorinated end group or not also indicate that fluorous interactions exist between *F*-hexane in the gas core and the fluorinated NPs and play a significant role in MB size and stability characteristics.

Table 2: Physical characteristics of DPPC microbubbles with dendronized IONPs

	DPPC	DPPC/ $C_2H_5OEG_8Den$	DPPC/ $C_2F_5OEG_8Den$	DPPC/ $C_4H_9OEG_8Den$	DPPC/ $C_4F_9OEG_8Den$
R_{mean} (optical, µm)	0.9 ± 0.1	1.6 ± 0.2	1.0 ± 0.2	1.4 ± 0.1	1.0 ± 0.2
R_{mean} (acoustical, µm)	0.8 ± 0.2	1.1 ± 0.2	0.9 ± 0.2	1.4 ± 0.2	1.2 ± 0.2
Half-life ($t_{1/2}$, h)	6.8 ± 0.5	3.6 ± 0.7	6.1 ± 0.9	1.3 ± 0.2	5.0 ± 0.9

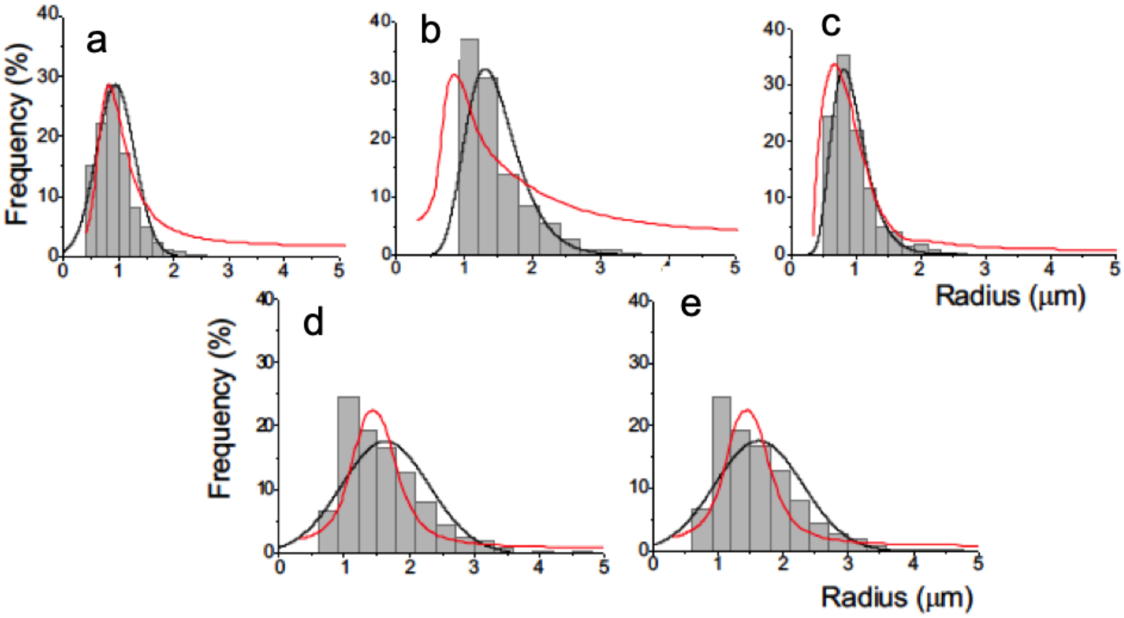

Figure 5: Size distributions of DPPC and DPPC/dendronized IONPs-shelled microbubbles stabilized with *F*-hexane (grey line: fit with a Gaussian function of the size histograms obtained from optical microscopy; red line: distributions obtained from the acoustical method). a) DPPC alone; b-e) DPPC/IONP@$C_nX_{2n+1}OEG_8$Den mixtures with b) $C_2H_5OEG_8$Den; c) $C_2F_5OEG_8$Den; d) $C_4H_9OEG_8$Den, and e) $C_4F_9OEG_8$Den. The concentration of IONPs was 0.1 mg mL^{-1}; temperature 25°C.

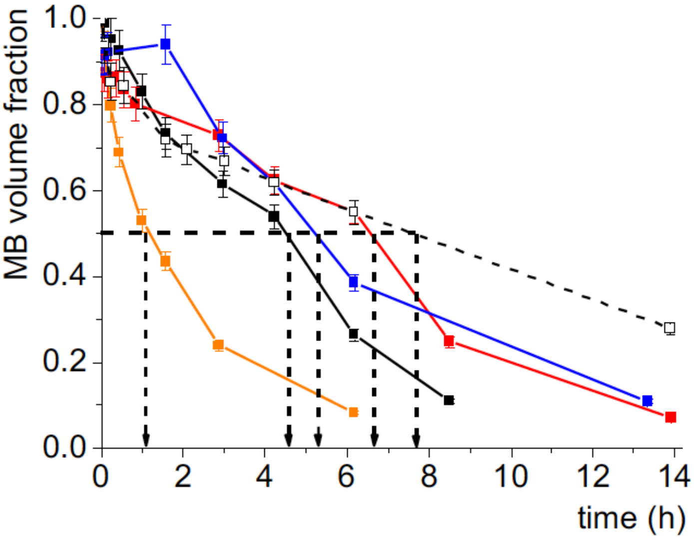

Figure 6. Time evolution (25°C) of the volume of DPPC microbubbles (dotted grey) and of DPPC microbubbles incorporating various IONPs: IONP@$C_2H_5OEG_8$ (black); IONP@$C_2F_5OEG_8$ (red); IONP@$C_4H_9OEG_8$ (orange); IONP@$C_4F_9OEG_8$ (blue).

AFM analysis of spin-coated films of DPPC, dendronized iron oxide nanoparticles and their mixtures

With the objective of understanding whether the dendronized IONPs are incorporated within the DPPC shell of the MBs or “seated” directly on the air/water interface, mixed films of phospholipid and nanoparticles were prepared by spin-coating on silicon wafers and their morphology investigated by atomic force microscopy (AFM) in Peak-Force tapping mode. We therefore selected $C_2F_5OEG_8$Den, the dendron that led to the smallest and most stable MBs. The hydrocarbon analog $C_2H_5OEG_8$Den was also investigated for comparison. The DPPC concentration was set in order to obtain a discontinuous DPPC film (*i.e.* DPPC domains), allowing measurement of the height of the film. The mean height of both IONP@$C_2F_5OEG_8$Den and IONP@$C_2H_5OEG_8$Den, is 10.0 ± 1.7 nm, as determined by statistic particles analysis (Fig. 7). Both IONPs are well dispersed without occurrence of aggregation.

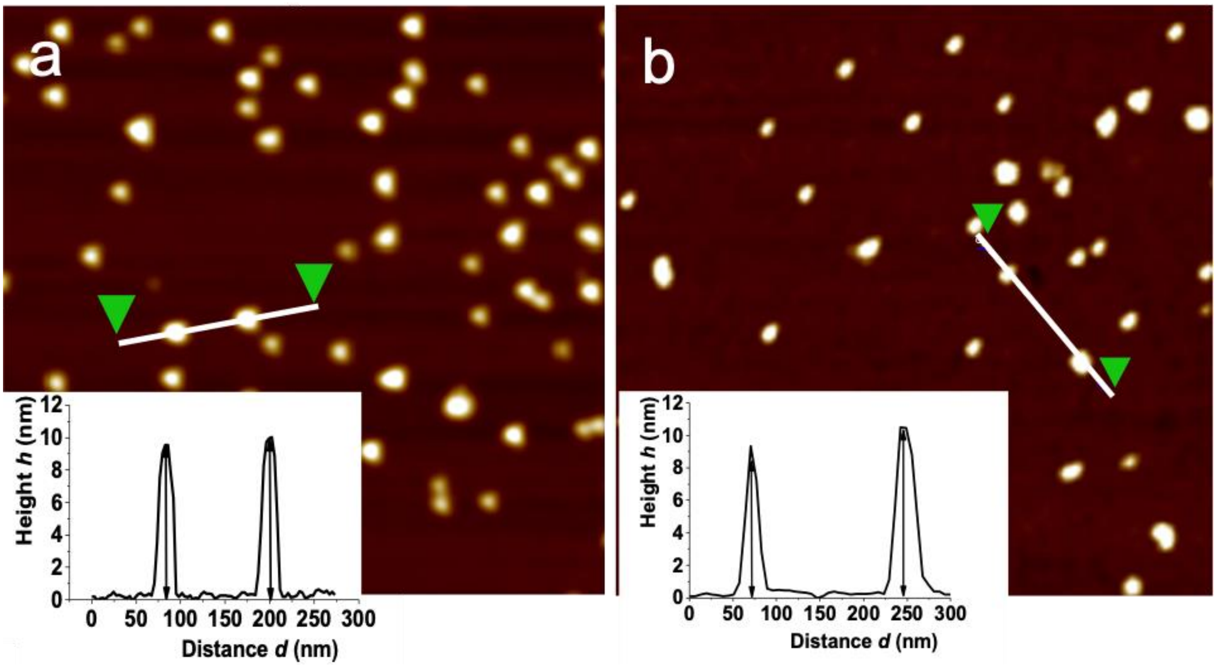

Figure 7. AFM topography images (1 x 1 µm) and height profiles of a) IONP@$C_2F_5OEG_8$Den and b) IONP@$C_2H_5OEG_8$Den. Dispersions of IONPs in ethanol (0.002 mg mL^{-1}) were spin-coated on silicon wafers.

The films of DPPC spin-coated on silicon wafers from ethanol dispersions were found to be formed of large domains of a monolayer in coexistence with small domains of a bilayer (Fig. 8a). The profile measured on the magnified image (Fig 8bc) shows that the heights of the monolayer and bilayer are 1.5 ± 0.3 nm and 5.0 ± 1.0 nm, respectively. These measurements are in agreement with earlier reports [29].

Figure 9A shows an AFM topography image of a mixed film of DPPC and IONP@$C_2F_5OEG_8$Den. The IONPs are seen to be preferentially located within the DPPC monolayer domains, while almost no particles were found directly on the wafer. The profile (Fig. 9Ac) measured on the magnified image (Fig. 9Ab) indicate that the fluorinated IONPs are embedded in the 1.5 nm-thick DPPC monolayer. A different morphology is observed for the mixed film of DPPC and IONPs grafted with the hydrogenated dendron $C_2H_5OEG_8$Den. In this case, the domains formed by DPPC bilayers (~5 nm) are omnipresent, with only rare occurrence of domains of monolayers (Fig. 9Ba). It is seen that IONP@$C_2H_5OEG_8$Den are preferentially located in the regions of the wafer that are devoid of phospholipid domains. The height profile measured on the magnification image (Fig. 9Bb) show two IONPs of (~10 nm) in height, clearly separated by a bilayer domain.

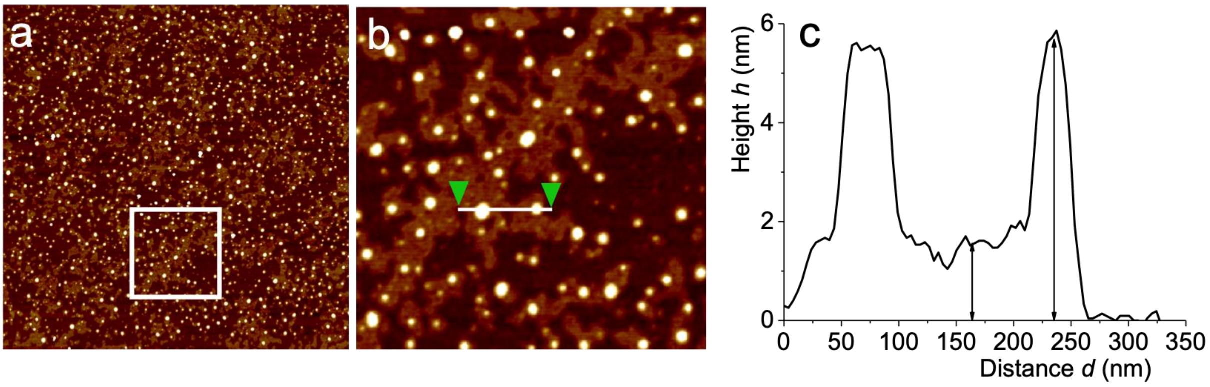

Figure 8. a) AFM topography image (4 x 4 µm) of a DPPC film spin-coated from an ethanol solution (0.5 mM); b) magnification (1 x 1 µm) of the square shown in a); c) height profile taken between the two green triangles in b).

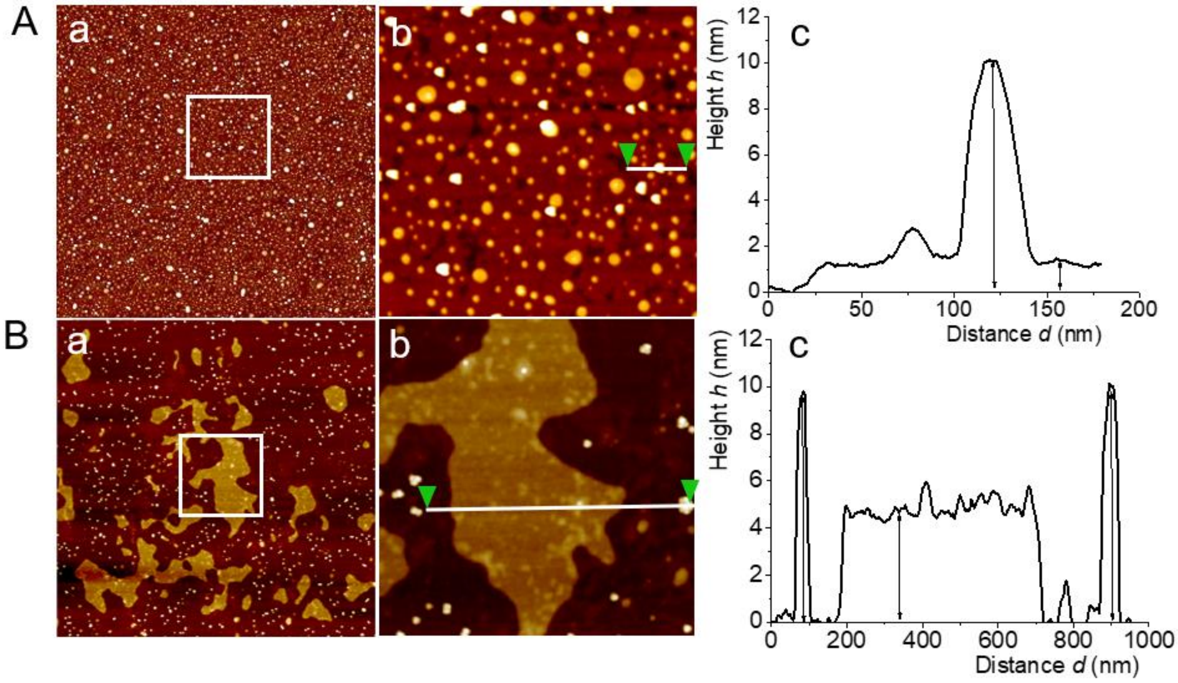

Figure 9. a) AFM topography image (4 x 4 µm) of mixed spin-coated films of DPPC and IONP@C_2F_5OEG$_8$Den (Panel A) and IONP@C_2H_5OEG$_8$Den (Panel B); b) magnification images (1 x 1 µm) of the white square shown in a); c) height profiles taken between the two green triangles in the corresponding image in b). Co-dispersions of DPPC (0.5 mM) and IONPs (0.002 mg mL^{-1}) in ethanol were spin-coated on silicon wafers.

This difference can be explained by the fact that short fluorinated groups such as C_2F_5 can increase the lipophilicity of molecules very significantly. This is the main reason why fluorine atoms, CF_3 or C_2F_5 groups are being introduced in the structure of many drugs, as they significantly improve their biodistribution [30]. These results tell us that the dendronized IONPs fitted with a C_2F_5 group have a higher affinity for the phospholipid film than those grafted with C_2H_5.

Conclusions and Perspectives

We report that small and highly stable magnetic microbubbles incorporating iron oxide nanoparticles in their phospholipid shells can be obtained by using iron oxide nanoparticles dendronized with oligoethylene glycol chains. The latter significantly increase the dispersibility of the nanoparticles in aqueous media.

We demonstrate that exposure to a supernatant fluorocarbon gas has a remarkable and considerable impact on the adsorption behavior of dendronized iron oxide nanoparticles and that the magnitude of this effect depends on the nature of the end group, fluorinated versus hydrogenated, of the dendron grafted on the nanoparticles. Introducing a short, fluorinated group at the end of the OEG chain was found to substantially increase the rate of adsorption of the nanoparticles at the interface, and even more so when exposed to *F*-hexane. A more compact film is observed when the film of nanoparticles is exposed to the fluorocarbon gas. This unexpected effect indicates that interactions develop between the dendron fluorinated end group and the fluorocarbon gas, within the mixed film at the interface.

As a consequence of this new phenomenon, small and stable fluorocarbon-stabilized microbubbles with a half-life of ~6 h can be obtained by admixing DPPC and iron oxide nanoparticles that are grafted with a C_2F_5-terminated dendron. The combined use of fluorinated dendrons and a supernatant fluorocarbon gas is a straightforward, effective method for preparing magnetic microbubbles, which could facilitate the development of future applications in medicine.

Finally, the AFM analysis of DPPC/iron oxide nanoparticles films indicates that the fluorinated IONPs offer an increased propensity for incorporation in phospholipid films than the hydrogenated ones, possibly due to increased lipophilic character.

Experimental Part

Materials

1,2-dipalmitoylphosphatidylcholine (DPPC) was purchased as a dry powder (99% purity) from Avanti Polar Lipids (Alabaster, AL) and used as received. Perfluorohexane (98% pure) was from Fluorochem. Pluronic F-68 (a poly(ethylene oxide)−poly(propylene oxide) triblock copolymer, MW ≈ 8300, purity >99%) and

HEPES (N-(2-hydroxyethyl)piperazine-N′-2-ethanesulfonic acid) were from Sigma-Aldrich (Lyon, France). A HEPES buffer solution (20 mmol L^{-1}) in a 150 mmol L^{-1} NaCl solution was prepared and its pH was adjusted to 7.4 with 1 N NaOH. Water was purified using a Millipore system (surface tension 71.4 mN m^{-1} at 20°C, resistivity 18.2 MΩ cm).

Synthesis of dendrons

The approach to the synthesis of dendrons $C_2F_5OEG_8Den$ and $C_4F_9OEG_8Den$ is described in [31]. From the intermediate D2-2P, the piperazine unit was installed in two steps (Fig. 10): 1) deprotection of *tert*-butyl group and 2) amide coupling by using HATU/DIPEA. Next, the removal of the carboxybenzyl group by hydrogenolysis allows introduction of the perfluoroalkyl chain via *N*-alkylation. Finally, treatment with trimethylsilylbromide produced the desired fluorinated bisphosphonate dendron.

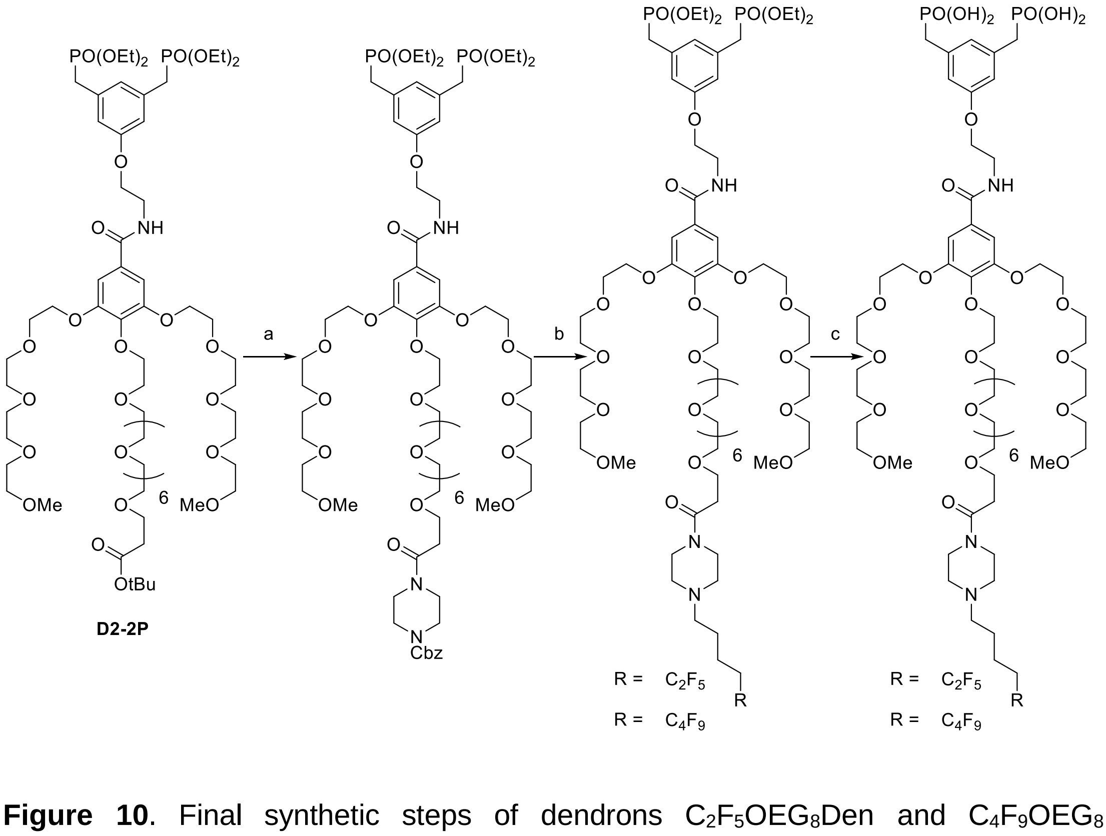

Figure 10. Final synthetic steps of dendrons $C_2F_5OEG_8Den$ and $C_4F_9OEG_8Den$. a) TFA/CH_2Cl_2, then piperazine-NCBz, HATU, DIPEA/DMF; 99% (2 steps); b) H_2, Pd/C/ MeOH, then perfluoroalkyliodide, K_2CO_3/CH_3CN; 80% for C_2F_5 and 55% for C_4F_9; c) $TMSBr/CH_2Cl_2$; 79% for C_2F_5 and 80% for C_4F_9.

$C_2F_5OEG_8Den$: **^{1}H NMR** (500 MHz, CD_3OD-*d_4*)**:** δ 7.25 (s, 2H), 6.84 (s, 1H), 6.79 (s, 2H), 4.22 (t, *J* = 4.5 Hz, 6H), 4.15 (t, *J* = 5.5 Hz, 2H), 3.87 (t, *J* = 4.7 Hz, 4H), 3.80 (t, *J* = 4.7 Hz, 2H), 3.76—3.50 (m, 52H), 3.33 (s, 6H), 3.12—3.09 (m, 2H), 3.03 (d, $^2J_{P-H}$ = 21.1 Hz, 4H), 2.65—2.62 (m, 2H), 2.27—2.16 (m, 2H), 1.88—1.82 (m, 2H), 1.68—1.62 (m, 2H) ppm. **^{13}C NMR** (125 MHz, CD_3OD-*d_4*)**:** δ 172.3, 169.5, 160.1, 153.8, 142.4, 136.6, 130.5, 115.3, 107.8, 73.6, 73.0, 71.9, 71.7—71.3 (several peaks), 70.8, 70.1, 68.5, 67.4, 62.2, 59.1, 57.3, 41.0, 39.6, 34.2, 24.2 ppm. **^{19}F NMR (**282 MHz, CD_3OD-*d_4*): δ -86.9, -119.4 ppm. **^{31}P NMR** (202 MHz, CD_3OD-*d_4*): δ 22.7 ppm.

$C_4F_9OEG_8Den$: **^{1}H NMR** (500 MHz, CD_3OD-*d_4*): δ 7.25 (s, 2H), 6.83 (s, 1H), 6.78 (s, 2H), 4.22 (t, *J* = 4.5 Hz, 6H), 4.14 (t, *J* = 5.6 Hz, 2H), 3.87 (t, *J* = 4.7 Hz, 4H), 3.80 (t, *J* = 4.6 Hz, 2H), 3.76—3.50 (m, 74H), 3.33 (s, 6H), 3.10—3.06 (m, 2H), 3.02 (d, $^2J_{P-H}$ = 21.0 Hz, 4H), 2.64—2.59 (m, 2H), 2.32—2.21 (m, 2H), 1.89—1.83 (m, 2H), 1.70—1.63 (m, 2H) ppm. **^{13}C NMR** (125 MHz, CD_3OD-*d_4*)**:** δ 172.3, 169.5, 160.1, 153.8, 142.4, 136.6, 130.5, 125.3, 115.3, 108.9, 79.3, 73.6, 73.0, 72.1, 71.9—71.3 (several peaks), 70.8, 70.0, 68.5, 67.4, 62.2, 59.1, 57.3, 52.9, 52.5, 43.7, 41.0, 39.6, 34.2, 30.8, 24.2, 18.7 ppm. **^{19}F NMR (**470 MHz, CD_3OD-*d_4*): δ -82.6, -115.6, -125.3, -127.1 ppm. **^{31}P NMR** (202 MHz, CD_3OD-*d_4*): δ 22.4 ppm.

Synthesis of dendronized iron oxide nanoparticles

The synthesis was adapted from an earlier report [21]. In a 100 mL two-necked flask, iron II stearate (2.2 mmol, 1.38 g), oleic acid (4.4 mmol, 1.24 g) and dioctylether (20 mL) were mixed together. The resulting solution was heated to 120°C for 1 h under magnetic stirring without reflux condenser. The magnetic stirrer was removed and the condenser connected to the flask. The solution was heated up to 298°C for 2 h with a heating rate of 5°C min^{-1}. After cooling, a black suspension was collected and precipitated by addition of acetone. Finally, the nanoparticles were washed three times with a mixture of $CHCl_3$/acetone (1:4). In a 30 mL vial, a nanoparticle suspension in THF (5 mg of iron) was introduced with the appropriate dendron (7 mg). The vial was filled with 25 mL of THF and the mixture was magnetically stirred for 24 h. The resulting nanoparticles were centrifuged after addition of cyclohexane, dispersed in water and separated by ultrafiltration.

Bubble profile analysis tensiometry

Axisymmetric bubble shape analysis was applied to a rising bubble of gas (air or *F*-hexane-saturated air) formed in a dispersion of dendronized IONPs in an aqueous phase (HEPES buffer). As described in [23], the variation of the interfacial tension during the process of adsorption of the dendronized IONPs at the gas/liquid interface acquired using a Tracker® tensiometer (Teclis, Civrieux d'Azergues, France). A 5 µL bubble was formed at the end of a steel capillary that had a tip diameter of 1 mm. The rising bubble was saturated with *F*-hexane by purging a 1 mL syringe trice with *F*-hexane-saturated air sampled above liquid *F*-hexane. This syringe was then mounted immediately on the tensiometer's injection cell of the tensiometer and the rising bubble was formed. The pressure and concentration of the *F*-hexane-saturated vapor at 25°C are 2.9 10^4 Pa and 11.66 mol m^{-3} [4]. IONP dispersions with Fe concentrations ranging from 0.1 to 10^{-4} mg mL^{-1} were obtained by diluting the 1 mg mL^{-1}-concentrated stem aqueous dispersions with HEPES buffer. The IONP@$C_4X_9OEG_8$Den (X = F and H) aqueous dispersions were sonicated for 30 min (setting 5) before tensiometric measurement. The sonicator (Vibracell, Bioblock Scientific, Illkirch, France) was equipped with a 3 mm titanium probe and operated at 20 kHz with an output power of ~600 W (duty cycle 40%).

Preparation of the microbubbles

DPPC (50 mmol L^{-1}) and Pluronic F-68 (DPPC/F-68 molar ratio 10:1) were dispersed in a non-degassed HEPES buffer solution (0.9 mL) in a sealed glass vial (inner diam. 13 mm, length 35 mm) by magnetic stirring for 3-6 h at 50°C. Pluronic F-68 was added to facilitate phospholipid dispersion and foam formation. 100 µL of the dendronized IONPs dispersion (Fe conc.: 1 mg mL^{-1}) were injected into the dispersion. The dispersions were sonicated under air in a sonication bath at 50°C for 30 min. In the case of NP@$C_4X_9OEG_8$Den (X = H or F), pre-sonication (2 min, setting 5) under air was applied. N_2 was allowed to bubble through three vials containing *F*-hexane before being flushed above the aqueous phase into the sealed glass vial during 3 min in order to saturate the gas phase with *F*-hexane. The resulting dispersions were treated using a VialMix shaker (Bristol-Myers Squibb, New York, NY) for 45 s under *F*-hexane-saturated N_2 at room temperature. The resulting foam was immediately diluted to 10 mL of HEPES buffer. Size fractionation of the microbubbles was achieved by flotation for 60 min.

Optical microscopy

A few droplets (three to four) of the bubble dispersion were positioned in a concave glass slide and covered with a glass slide. The samples were observed using a Nikon Eclipse 90i microscope (transmission mode). Rapid image acquisition was obtained with a Lumenera Infinity 2 charge-coupled device (CCD) camera (Lumenera, Ottawa, Canada). The mean radii of the bubbles were determined using ImageJ on 5−10 slides.

Acoustic size determination

The method exploits the sound attenuation undergone by multi-frequency ultrasound waves that propagate through the aqueous bubble dispersion. Standard simple-harmonic resonator curves are fitted to measured attenuations in order to infer the size of the bubbles. A low-power emitter is used so as to avoid alteration of the bubble characteristics and stability. For experimental details see [32]. Each measurement was repeated three times on different bubble preparations. The volume of microbubble dispersion injected in the acoustic cell was 2 mL.

AFM topography analysis of mixed films of DPPC and dendronized IONPs

Thin films of DPPC, dendronized IONPs and DPPC/dendronized IONPs mixtures were prepared by spin-coating on silicon wafers [33]. A dispersion of dendronized IONPs in water (1 mg L^{-1}) was freeze-dried and then dissolved in ethanol for preparing a 0.1 mg mL^{-1}-concentrated dispersion. 40 µL of this dispersion were added to 2 mL of a 1 mM-concentrated DPPC ethanol solution in order to obtain a mixed DPPC/dendronized IONP spin-coated film that has the same DPPC/Fe molar ratio as that used for the preparation of the microbubbles (28:1). A 0.5 mM-concentrated mixed dispersion was obtained by diluting this 1 mM dispersion. Silicon wafers were cleaned for 30 min in a sonication bath containing ethanol/milli Q water (1:1 vol.), followed by 2 min in a plasma cleaner. A droplet (15 µL) of DPPC, dendronized IONPs or mixed DPPC/dendronized IONPs dispersions was deposited on silicon wafers and immediately spun for 1 min at 3000 rpm (Spin150 from SPS, Semiconductor Production Systems Europe). The spin-coated samples were placed under vacuum in a desiccator during 15-20 h to fully evaporate the solvents. The silicon wafers were stored at 4°C until the AFM measurement. AFM images were obtained by scanning the spin-coated films using the Dimension AFM Icon (Bruker) operated in Peak-Force tapping mode. Peak-Force AFM is based on Peak Force tapping technology, in which the probe is oscillated in a similar way as in the tapping mode, but at far lower resonance frequency. Each time the tip and the sample are brought together, a force curve is captured. Ultra-sharp silicon tips on nitride lever were used (Bruker, ScanAsyst with a spring constant of 0.4 N m^{-1} and tip radius of ~5 nm). During AFM imaging, the force was reduced in order to avoid dragging of molecules by the tip. All analyses of the images were conducted in integrated software. At least three different samples were analyzed and several positions were scanned on the silicon wafer for each sample. The error on measurements along the z axis was estimated at ± 0.5 nm.

Acknowledgements

The authors acknowledge the European Regional Development Fund (ERDF) in the framework of the INTERREG V Upper Rhine program “Transcending borders with every project” for financing the NANOTRANSMED project, including Ph.D. (D.S. and F.P.) and post-doc (D.-V. N. and J.W.) scholarships. J.W acknowledges the CNRS GIS Fluor for a travel grant.

References

1. Chong, W. K.; Papadopoulou, V.; Dayton, P. A. *Abdom. Radiol.* **2018**, *43*, 762–772; Jain, A.; Tiwari, A.; Verma, A.; Jain, S. K. *Drug Deliv. Transl. Res.* **2018**, *8*, 150-164; Wang, S.; Hossack, J.; Klibanov, A. L. *J. Drug Target.* **2018**, *26*, 420-434; Lindner, J. R. *Nat. Rev. Drug Disc.* **2004**, *3*, 527-532; Wheatley, M. A.; Forsberg, F.; Dube, N.; Patel, M.; Oeffinger, B. E. *Ultrasound Med. Biol.* **2006**, *32*, 83-93; Klibanov, A. L. *Med. Biol. Eng. Comput.* **2009**, *47*, 875-882; Stride, E.; Edirisinghe, M. J. *Med. Biol. Eng. Comput.* **2009**, *47*, 809-811; Rychak, J. J.; Klibanov, A. L. *Adv. Drug Delivery Rev.* **2014**, *72*, 82-93; Sirsi, S. R.; Borden, M. A. *Theranostics* **2012**, *2*, 1208-1222; Ferrara, K. W.; Borden, M. A.; Zhang, H. *Acc. Chem. Res.* **2009**, *42*, 881-892.
2. Aw, M. S.; Paniwnyk, L.; Losic, D. *Expert Opin. Drug Deliv.* **2016**, *13*, 1383-96; Song, K.-H.; Harvey, B. K.; Borden, M. A. *Theranostics* **2018**, *8*, 4393-4408.
3. Schutt, E. S.; Klein, D. H.; Mattrey, R. M.; Riess, J. G. *Angew. Chem. Int. Ed.* **2003**, *42*, 3218-3235.
4. Kabalnov, A.; Bradley, J.; Flaim, S.; Klein, D.; Pelura, T.; Peters, B.; Otto, S.; Reynolds, J.; Schutt, E.; Weers, J. *Ultrasound Med. Biol.* **1998**, *24*, 751-760.

5. Kabalnov, A.; Klein, D.; Pelura, T.; Schutt, E.; Weers, J. *Ultrasound Med. Biol.* **1998**, *24*, 739-749.

6. Szijjarto, C.; Rossi, S.; Waton, G.; Krafft, M. P. *Langmuir* **2012**, *28*, 1182-1189.

7. Ando, Y.; H. Tabata; Sanchez, M.; Cagna, A.; Koyama, D.; Krafft, M. P. *Langmuir* **2016**, *32*, 12461-12467.

8. Yang, F.; Li, Y.; Chen, Z.; Zhang, Y.; Wu, J.; Gu, N. *Biomaterials* **2009**, *30*, 3882-3890 ; Park, J. I.; Jagadeesan, D.; Williams, R.; Oakden, W.; Chung, S.; Stanisz, G. J.; Kumacheva, E. *ACS Nano* **2010**, *4*, 6579-6586 ; Liu, Z.; Lammers, T.; Ehling, J.; Fokong, S.; Bornemann, J.; Kiessling, F.; Gätjens, J. *Biomaterials* **2011**, *32*, 6155-6163.

9. Mulvana, H.; Eckersley, R. J.; Tang, M.-X.; Pankhurst, Q.; Stride, S. *Ultrasound Med. Biol.* **2012**, *38*, 864-875; Stride, E.; Porter, C.; Prieto, A. G.; Pankhurst, Q. *Ultrasound Med. Biol.* **2009**, *35*, 861-868.

10. Lammers, T.; Koczera, P.; Fokong, S.; Gremse, F.; Ehling, J.; Vogt, M.; Pich, A.; Storm, G.; Zandvoort, M.; Kiessling, F. *Adv. Funct. Mater.* **2015**, *25*, 36-43.

11. Unger, E. C.; McCreery, T. P.; Sweitzer, R. H.; Caldwell, V. E.; Wu, Y. *Invest. Radiol.* **1998**, *33* (12), 886-892.

12. Vlaskou, D.; Pradhan, P.; Bergemann, C.; Klibanov, A. L.; Hensel, K.; Schmitz, G.; Plank, C.; Mykhaylyk, O. *AIP Conf. Proc.* **2010**, *1311*, 485-494; Plank, C.; Vlaskou, D.; Schillinger, U.; Mykhaylyk, O. *Ther. Deliver.* **2011**, *2*, 717-726; Mannell, H.; Pircher, J.; Folcher, F.; Stampnik, Y.; Räthel, T.; Gleich, B.; Plank, C.; Mykhaylyk, O.; Dahmani, C.; Wörnle, M.; Ribeiro, A.; Pohl, U.; Krötz, F. *Nanomed. Nanotech. Biol. Med.* **2012**, *8*, 1309-1318.

13. Nguyen, P. N.; Nikolova, G.; Polavarapu, P.; Waton, G.; Phuoc, L. T.; Pourroy, G.; Krafft, M. P. *RSC Adv.* **2013**, *3*, 7743-7746.

14. Owen, J.; Crake, C.; Lee, J. Y.; Carugo, D.; Beguin, E.; Khrapitchev, A. A.; Browning, R. J.; Sibson, N.; Stride, E. *Drug Deliv. Transl. Res.* **2018**, *8*, 342–356.

15. Daou, T. J.; Pourroy, G.; Greneche, J. M.; Bertin, A.; Felder-Flesch, D.; Begin-Colin, S. *Dalton Trans.* **2009**, *23*, 4442-49.

16. Basly, B.; Felder-Flesch, D.; Perriat, P.; Billotey, C.; Taleb, J.; Pourroy, G.; Begin-Colin, S. *Chem. Commun.* **2010**, *46*, 985-987.

17. *Dendrimers in Nanomedecine*. Ed: Felder-Flesch, D.; Pan Stanford Publishing Pte. Ltd.: Singapore, 2016.

18. Casset, A.; Jouhannaud, J.; Garofalo, A.; Spiegelhalter, C.; Nguyen, D.-V.; Felder-Flesch, D.; Pourroy, G.; Pons, F. *Int. J. Pharm.* **2019**, *556*, 287-300.

19. Garofalo, A.; Parat, A.; Bordeianu, C.; Ghobril, C.; Kueny-Stotz, M.; Walter, A.; Jouhannaud, J.; Begin-Colin, S.; Felder-Flesch, D. *New. J. Chem.* **2014**, *38*, 5226-5239.

20. Sun, S.; Zeng, H.; Robinson, D. B.; Raoux, S.; Rice, P. M.; Wang, S. X.; Li, G. *J. Am. Chem. Soc.* **2004**, *126*, 273-79.

21. Walter, A.; Billotey, C.; Garofalo, A.; Ulhaq-Bouillet, C.; Lefèvre, C.; Taleb, J.; Laurent, S.; Elst, L. V.; Muller, R. N.; Lartigue, L.; Gazeau, F.; Felder-Flesch, D.; Begin-Colin, S. *Chem. Mater.* **2014**, *26*, 5252−5264.

22. Nguyen, P. N.; Veschgini, M.; Tanaka, M.; Waton, G.; Vandamme, T.; Krafft, M. P. *Chem. Commun.* **2014**, *50*, 11576-11579; Shi, D.; Liu, X.; Counil, C.; Krafft, M. P. *Langmuir* **2019**, *DOI: 10.1021/acs.langmuir.8b03546*.

23. Nguyen, P. N.; Trinh Dang, T. T.; Waton, G.; Vandamme, T.; Krafft, M. P. *ChemPhysChem* **2011**, *12*, 2646-2652.

24. Gazzera, L.; Milani, R.; Pirrie, L.; Schmutz, M.; Blanck, C.; Resnati, G.; Metrangolo, P.; Krafft, M. P. *Angew. Chem. Int. Ed.* **2016**, *55*, 10263-10267.

25. Yang, G.; O'Duill, M.; Gouverneur, V.; Krafft, M. P. *Angew. Chem. Int. Ed.* **2015**, *54*, 8402-8406.

26. Justeau, C.; Vela-Gonzalez, A. V.; Jourdan, A.; Riess, J. G.; Krafft, M. P. *ACS Sustain. Chem. Eng.* **2018**, *6*, 11450-11456.

27. Gladysz, J. A.; Curran, D. P.; Horváth, I., *Handbook of Fluorous Chemistry*. Wiley-VCH: Weinheim, 2004.

28. Luo, Z.; Zhang, Q.; Oderaotoshi, Y.; Curran, D. P. *Science* **2001**, *291*, 1766-1769; Dinh, L. V.; Gladysz, J. *Angew. Chem. Int. Ed.* **2005**, *44*, 4095-4097.

29. Jurak, M.; Chibowski, E. *Langmuir* **2007**, *23*, 10156-10163.

30. Wang, J.; Sánchez-Roselló, M.; Aceña, J. L.; Pozo, C. d.; Sorochinsky, A. E.; Fustero, S.; Soloshonok, V. A.; Liu, H. *Chem. Rev.* **2014**, *114*, 2432−2506.

31. Nguyen, D.-V.; Hugoni, L.; Filippi, M.; Perton, F.; Shi, D.; Voirin, E.; Power, L.; Cotin, G.; Krafft, M. P.; Scherberich, A.; Lavalle, P.; Begin-Colin, S.; Felder-Flesch, D. *ChemPlusChem, submitted* **2019**.

32. Rossi, S.; Waton, G.; Krafft, M. P. *Langmuir* **2010**, *26*, 1649-1655.

33. Simonsen, A. C.; Bagatolli, L. A. *Langmuir* **2004**, *20*, 9720-9728.